Accepted for Publication in The Holocene on July 22, 2016

1 **Late Holocene Indian summer monsoon variability revealed from a 3,300-year-long**

2 **lake sediment record from Nir'pa Co, southeastern Tibet**

3

4 Broxton W. Bird[1], Yanbin Lei[2,3], Melanie Perello[1], Pratigya J. Polissar[4], Tandong Yao[2,3],

5 Bruce Finney[5], Daniel Bain[6], David Pompeani[6] and Lonnie G. Thompson[7]

6

7 [1]Department of Earth Sciences, Indiana University-Purdue University, Indianapolis, IN

8 46208, USA.

9 [2]Key Laboratory of Tibetan Environment Changes and Land Surface Processes Institute

10 of Tibetan Plateau Research, Chinese Academy of Sciences, Beijing, 100101, China.

11 [3] CAS Center for Excellence in Tibetan Plateau Earth System, Beijing, 100101, China.

12 [4]Lamont Doherty Earth Observatory, Columbia University, New York, NY10964, USA.

13 [5]Department of Biological Sciences, Idaho State University, Pocotello, ID 83209, USA.

14 [6]Department of Geology and Environmental Science, University of Pittsburgh,

15 Pittsburgh, PA, 15260, USA.

16 [7]Byrd Polar Research Center, The Ohio State University, Columbus, OH 43210, USA.

17

20

21 **Abstract**

22 Sedimentological and geochemical results from Nir'pa Co, an alpine lake on the

23 southeastern Tibetan Plateau detail late Holocene ISM hydroclimate during the last 3,300

24 years. Constrained by modern calibration elevated silt and lithics and low sand and clay

25 between 3.3-2.4 ka and 1.3 ka to the present indicate two pluvial phases with lake levels

26 near their current overflow elevation. Between 2.4-1.3 ka, a sharp increase in sand and

27 corresponding decrease in lithics and silt suggest drier conditions and lower lake levels at

28 Nir'pa Co. Hydroclimate expressions in the sedimentological proxies during the

29 Medieval Climate Anomaly (MCA) and Little Ice Age (LIA) are not statistically

30 significant, suggesting that these events were minor compared to the millennial scale

31 variability on which they were superimposed. However, decreasing sand and increasing

32 lithics and silt during the MCA between 950-800 cal yr B.P. may suggest briefly wetter

33 conditions while increasing sand and reduced lithics and silt from 500-200 cal yr B.P.

34 suggest potentially drier conditions during the LIA. Similarities with regional records

35 from lake, ice core and speleothem records from the central and eastern Tibetan Plateau,

36 India, and the Arabian Sea, suggest generally coherent late Holocene ISM variability in

37 these regions. Increased late Holocene ISM intensity occurred during times when Tibetan

38 Plateau surface air temperatures were warmer, Indo-Pacific sea surface temperatures

39 were elevated, and the tropical Pacific was in a La Niña-like mean state. Conversely,

40 aridity between 2.4-1.3 ka occurred in concert with cooling on the Tibetan Plateau and in

41 the Indo-Pacific with more El Niño-like conditions in the tropical Pacific. Differences

42 with western Tibetan records may reflect a weakened ISM and stronger westerlies in this

43 region during the late Holocene.

44

45 **1. Introduction**

46   Holocene paleoclimate records from the Tibetan Plateau and surrounding regions,

47   an area referred to as the Third Pole Environment (Qiu, 2008), show that the Indian

48   summer monsoon (ISM) reached a maximum during the early and middle Holocene

49   between 10 and approximately 6 ka when boreal summer insolation peaked and strong

50   tropical Pacific sea surface temperature (SST) gradients resembled a La Niña-like mean

51   state (Koutavas et al., 2006; He et al., 2004; Bird et al., 2014; Cai et al., 2012; Yanhong

52   et al., 2006; Marchitto et al., 2010; Morrill et al., 2003). The late Holocene, in contrast,

53   has been characterized by increasing aridity as summer insolation waned and an

54   increasingly El Niño-like mean state developed in the tropical Pacific. Despite an

55   improved understanding of long-term Holocene ISM trends and the likely driving

56   mechanisms, higher frequency ISM variations have been more difficult to characterize

57   because there are comparatively few high-resolution records from the Third Pole (Chen et

58   al., 2015). The late Holocene is under represented by high-resolution paleoclimate

59   records in part because mean state aridity resulted in decreased resolution (e.g., Bird et

60   al., 2014) or depositional hiatuses in many ISM archives (Berkelhammer et al., 2012;

61   Morrill et al., 2006; Cai et al., 2012). The paucity of climate records detailing ISM

62   variability during the last few millennia limits our understanding of monsoon dynamics

63   during a time when climatic boundary conditions were generally similar to the present,

64   but perturbations in radiative and other forcings, including ocean-atmosphere processes,

65   produced widely recognized climatic events including: the Medieval Climate Anomaly

66   (MCA; 950-1250 AD) and Little Ice Age (LIA; 1450-1900 AD)(Mann et al., 2009).

67   Paleoclimate records from the Third Pole that span at least part of the late

68   Holocene suggest that within this period of general aridity there were regional scale

69   fluctuations in ISM precipitation, lake levels and temperature (Bird et al., 2014;

70   Herzschuh et al., 2006; Mischke and Zhang, 2010). Similar variability observed on longer

71   timescales in Holocene-length paleoclimate records suggest that sub-orbital climate

72   changes may be influenced by a variety of direct and indirect factors, including solar

73   variability (Cai et al., 2012), Atlantic and Indo-Pacific ocean-atmosphere teleconnections

74   (Chen et al., 2015; Bird et al., 2014; Hong et al., 2003; Goswami et al., 2006), and

75   Tibetan Plateau surface air temperatures (Bird et al., 2014). At Paru Co, an alpine lake in

76   the monsoon dominated southeastern Tibetan Plateau, Bird et al. (2014) noted that low

77   lake stands and high hydrogen isotopic compositions of sedimentary leaf waxes (δD_{wax})

78   coincided with warmer Indo-Pacific SST (Koutavas et al., 2006; Stott et al., 2004), cooler

79   eastern equatorial Pacific SST (Marchitto et al., 2010) and elevated surface air

80   temperatures on the central Tibetan Plateau (Herzschuh et al., 2006). The opposite

81   associations were noted during low lake stands. Late Holocene aridity on the Third Pole

82   occurred within the context of more El Niño-like Pacific SST structure and cooling over

83   the Tibetan Plateau (Bird et al., 2014). Centennial lake level variability followed this

84   general warm-wet, cool-dry pattern. Persistently low lake levels at Paru Co during the

85   late Holocene, however, limited the lake's sensitivity to hydroclimate changes, making it

86   difficult to discern ISM variability at centennial or shorter time scales. Because many

87   other records also lose resolution during this time, the role that regional SAT and/or Indo-

88   Pacific SST played in ISM variability during the last ~4000 years is not well defined.

89   Filling this gap in knowledge is important because changes in radiative forcing and

90   ocean-atmosphere systems, particularly during the MCA and LIA, have been suggested

91   to have produced significant precipitation anomalies in the East Asian and South

92   American monsoon systems (Zhang et al., 2008; Bird et al., 2011; Chen et al., 2015). In

93   the ISM region, however, hydroclimatic signatures of the MCA and LIA in paleoclimate

94   records are more equivocal. Some records, such as accumulation at Dasuopu (Thompson

95   et al., 2000) and $\delta^{18}O$ from Dandak Cave (India; Sinha et al., 2006) and Sahiya Cave

96   (Sinha et al., 2015), suggest possibly wetter conditions during the MCA and drier

97   conditions during the LIA, while other studies suggest the opposite (Liu et al., 2009).

98   Excluding the Third Pole, the MCA and LIA appear to have produced an east-west

99   hydroclimate dipole response north of 30ºN whereby northwest and central Asia were

100   drier and northern to northeastern China wetter during the MCA (Chen et al., 2015). The

101   opposite conditions are suggested for the LIA. In order to help resolve questions

102   regarding late Holocene ISM dynamics and their relationships with hydroclimate

103   variability across Asia, additional records from core ISM regions are needed.

104   To this end, we present a 3,300-year-long multi-proxy hydroclimate record from

105   Nir'pa Co that details the hydroclimatic variability of a region highly sensitive to changes

106   in ISM precipitation. Through comparison with existing paleoclimate records from the

107   Third Pole and other climatically significant regions, we investigate the regional

108   expression of late Holocene ISM precipitation (including the MCA and LIA), its

109   relationship with known climatic and ocean-atmosphere influences and whether Indo-

110   Pacific and ENSO-like forcing mechanisms of ISM variability suggested for the early and

111   middle Holocene can similarly account for late Holocene ISM variations.

112   [Insert Figure 1]

113   *1.1 Study Area: Nir'pa Co*

114   Nir'pa Co is a small (0.1 km^2) alpine lake situated at 4775 m above sea level (asl)

115   in the Nyanchentangula Mountains on the southeastern Tibetan Plateau (Fig. 1, 2a; N

116   29.734º, E 92.386º). Nir'pa Co's watershed is defined by a 5.38 km-long and 1.3 km-

117   wide glacially carved valley that trends northwest-southeast with a maximum elevation of

118   5150 m asl (Fig. 2a). This valley is part of a larger plateau that contains numerous glacial

119   features, such as moraines and glacial lakes, including Paru Co (Bird et al., 2014). The

120   local bedrock is geologically homogeneous, consisting of Pleistocene age andesite

121   (Choubert et al., 1983). The lake is deep relative to others in the area, with a maximum

122   depth of 18.6 m. Nir'pa Co's bathymetry is generally steep sided with a flat bottom that

123   is deepest near the center of the lake (Fig. 2b). An ephemeral stream enters on the lake's

124   northwestern shore, at which point it forms a delta on a shallow littoral shelf (Fig. 2b). A

125   channel at the lake's southeast shore provides an outlet for overflow that has incised into

126   the terminal glacial moraine that dams the lake. This outlet was overflowing, albeit with

127   restricted flow, when cores were collected from Nir'pa Co in May 2011 and June 2015,

128   suggesting that the lake is currently at or near its maximum surface elevation but

129   becomes seasonally restricted.

130   [Insert Figure 2]

131   Indian summer monsoon moisture largely derived from the Bay of Bengal is the

132   primary source of precipitation for regions of the Tibetan Plateau between the Himalayan

133   and Tanggula Mountains and for interior monsoonal regions in India (Tian et al., 2001;

134   Tian et al., 2007; Sinha et al., 2015). Consistent with this, 92 % of mean annual

135   precipitation at Nir'pa Co occurs during the monsoon season with peaks between May

136   and September when temperatures rise above freezing and the lake is ice free and

137   sediment can be transported from the watershed and deposited in Nir'pa Co (Fig. 2c;

138   Peterson and Vose, 1997; Lawrimore et al., 2011; Bird et al., 2014). Precipitation during

139   the remainder of the year accounts for only 8 % of the annual hydrologic budget and is

140   received primarily as snow when average monthly temperatures are near or below 0ºC

141   from November through April. During these months, Nir'pa Co is covered with ice,

142   limiting sediment input to the lake. Tropical Rainfall Measuring Mission (TRMM –

143   3B43) precipitation data estimates suggest regional annual rainfall totals 1118 mm yr^{-1}

144   while instrumental weather station data indicate annual rainfall amounts to 479 mm yr^{-1}.

145   The difference between these amounts may be due in part to over estimations of rainfall

146   at elevation by TRMM data and underestimations of rainfall at elevation based on rainfall

147   gauge measurements made in valleys. Regardless, the majority of precipitation at Nir'pa

148   Co in either data set occurs during the summer monsoon season when the lake is ice-free

149   and sediment can be mobilized from the lake's catchment and transported to Nir'pa Co

150   via fluvial processes.

151   A number of ocean-atmosphere and terrestrial climate feedbacks influence ISM

152   precipitation (Peings and Douville, 2010; Ashok et al., 2004; Shaman and Tziperman,

153   2005). Interannual Indo-Pacific ocean-atmosphere variability associated with the El

154   Niño-Southern Oscillation (ENSO) is a primary modulator of ISM rainfall (Ashok et al.,

155   2004; Gadgil, 2003; Kumar et al., 2006; Krishnamurthy and Kirtman, 2009).

156   Observational records show that cooling in the Indo-Pacific during warm El Niño events

157   coincides with increased atmospheric subsidence and reduced precipitation over the

158   Asian monsoon region. During cool La Niña events, warm Indo-Pacific SST enhance

159   convergence and vertical air motion over the Asian monsoon region, thereby contributing

160 to enhanced monsoon rainfall. ENSO-like mechanisms have been invoked on longer

161 timescales to explain multi-decadal to millennial trends in ISM and Asian monsoon

162 rainfall, whereby persistent El Niño or La Niña-like conditions in the tropical Pacific

163 created background conditions of either persistently stronger or weaker monsoon

164 circulation over Asia (Bird et al., 2014; Hong et al., 2005; Krishnan and Sugi, 2003).

165   The Indian Ocean Dipole (IOD) is another recognized driver of ISM variability,

166 which may also contribute to long-term trends in monsoon rainfall (Ashok et al., 2004).

167 The IOD, however, is not wholly independent from ENSO and is considered by some to

168 be an extension of ENSO variability in the Indian Ocean, albeit with some independent

169 behavior (Ashok et al., 2001; Ashok et al., 2004). Warm IOD events are typically

170 associated with La Niñas and enhanced ISM rainfall. Cool IOD events are conversely

171 associated with El Niño events and reduced ISM rainfall. The IOD's influence on ISM

172 rainfall during the Holocene is not well known, however, because there are a limited

173 number of SST reconstructions from key centers of IOD action in the Indian Ocean and

174 none that continuously span the late Holocene.

175

176 **2. Methods**

177 *2.1 Sediment core and sample collection*

178   A 90 cm surface core (A-11) was collected from Nir'pa Co in May 2011 in 17.5

179 meters of water using an Aquatic Research hammer core (Fig. 2b). Two additional

180 surface cores (A-15 & B-15) were acquired in June 2015 using a piston coring system in

181 water depths of 16.5 and 1.0 m, respectively (Fig. 2b). The top 10 cm of A-11 were

182 extruded at 0.5 cm intervals in the field immediately following collection. Cores A-15

183 and B-15 were not extruded in the field, but instead secured with absorbent foam, which

184 stabilized the sediments for transport. Visible stratigraphy in the upper portion of B-15

185 and the lack of void space in A-15 indicated that the sediments didn't mix during

186 transport. In order to characterize modern sediment distributions, grab samples of the

187 upper 2 cm were collected using an Ekman grab sampler along a southeast-northwest

188 transect that extended from the lake's profundal zone (18 m) to the inlet (0.6 m; Fig. 2b).

189 All cores and grab samples were stored at 4ºC until they were analyzed at the Indiana

190 University-Purdue University, Indianapolis (IUPUI) Paleoclimatology and

191 Sedimentology Laboratory.

192

193 *2.2 Initial core description*

194   Surface cores were split, described, imaged and volumetrically subsampled (1 cm^{-3}

195 ^{3}) at 2 cm intervals for % water, dry bulk density and loss on ignition (LOI). Magnetic

196 susceptibility (MS) was measured on the archive half of the cores using a Bartington

197 MS2 magnetic susceptibility meter with units SI x10^{-5}. Wet 1 cm^{3} samples were weighed,

198 dried for 24 hours at 60ºC and reweighed to determine dry bulk density (ρ_{dry}; g cm^{-3}) and

199 % water. Percent total organic matter (% TOM) and carbonate (% TC) were determined

200 by weight loss after combustion at 550ºC (4 hours) and 1000ºC (2 hours), respectively

201 (modified from Heiri et al., 2001).

202

203 *2.3 Grain size*

204   Approximately 1.0 g of wet sediment was collected from homogenized grab

205 samples and at 1 cm intervals from surface cores A-11, dried for 24 hours at 60ºC and

206   weighed. Organic matter was removed prior to grain size analysis by soaking samples in

207   a 50 ml aliquot of 35 % H_2O_2 at room temperature for 24 hours before being treated

208   sequentially with five 20 ml aliquots of 35 % H_2O_2 at 65ºC (Gray et al., 2010). Biogenic

209   silica was removed with a 20 ml 1N NaOH digestion (6 hr at 60ºC) and verified by smear

210   slide for 10 % of the samples. Acid washing was not performed because LOI indicated

211   that carbonate was not present. After freeze drying, the samples were soaked for 24 hours

212   in a 2.5 % sodium metaphosphate solution. Particle size distributions of the lithic fraction

213   were measured using a Malvern Mastersizer 2000 with reported values calculated using

214   the average of three replicate measurements.

215

216   *2.4 Elemental and isotopic or organic carbon and sedimentary nitrogen*

217   Homogenized subsamples at ~2 cm intervals (n = 41) from core A-11 were

218   analyzed for total organic carbon (TOC), total nitrogen (TN) concentrations, and $\delta^{13}C$

219   and $\delta^{15}N$ using a Costech ECS 4010 elemental analyzer interfaced to a Thermo Delta V

220   Advantage continuous flow isotope ratio mass spectrometer. Isotope ratios are reported in

221   per mil units (‰) according to the relationship $\delta X = [(R_{sample} / R_{standard}) - 1] \cdot 1000$, where

222   X is the element of interest and R a measured isotopic ratio of either a sample or a

223   standard. Carbon isotope measurements are relative to the Vienna Peedee Belemnite

224   (VPDB) standard and all nitrogen measurements are relative to atmospheric nitrogen.

225   Replicate measurements of internal standards run during sample analysis yielded

226   coefficients of variation of 4.4 %, 6.9 %, for TOC and TN, respectively, and precision

227   better than 0.2 ‰ for the isotopic data. Isotope measurements were made at Idaho State

228   University.

229

230   *2.5 Biogenic silica and % lithics*

231   Biogenic silica was quantitatively determined on samples at ~ 2 cm resolution (n

232   = 41) from A-11 using a wet-alkali dissolution method (0.1M Na_2CO_3 at 85ºC for 5 hr)

233   modified from Mortlock and Froelich (1989) and measured by molybdate-blue

234   spectrophotometry. Values are reported as 10 % hydrated silica ($SiO_2 \cdot 0.4\ H_2O$) using a

235   multiplier of 2.4 times the weight percent of biogenic silica content (Mortlock and

236   Froelich, 1989). An estimated error of <4.6 % (calculated as the coefficient of variation)

237   is based on replicate measurements of two internal sediment standards.

238   The lithic abundance was calculated by subtracting percent abundances of

239   biogenic silica and % TOM from 100 % assuming that carbonate was not a significant

240   sediment constituent based on LOI data.

241

242   *2.6 Scanning X-ray Fluorescence Geochemistry*

243   Sedimentary titanium (Ti) concentrations were determined by scanning X-ray

244   fluorescence using an ITRAX XRF scanner at the University of Minnesota, Duluth (See

245   Supplemental Information for concentrations of other elements measured). Measurements

246   were made at 0.5 cm increments with a molybdenum X-ray tube and a sample exposure

247   time of 15 seconds per spot. Values are reported as counts per second (cps) where greater

248   elemental concentrations correspond to higher cps.

249

250   *2.7 Geochemistry*

251   Two samples composed of bedrock and glacial till from the adjacent Paru Co

252   watershed and one of bedrock from the Nir'pa Co watershed were analyzed by ALS

253   Global for a suite of elements, of which only Ti is discussed here (See supplemental

254   materials for other elements measured and concentrations). Following ultra-trace level

255   method ME-MS61, approximately 0.25 g of sample were digested using perchloric, nitric

256   and hydrofluoric acids with the residue leached with dilute hydrochloric acid and diluted

257   to volume. Measurements were made by inductively coupled plasma-atomic emission

258   spectrometry and inductively coupled plasma-mass spectrometry with results corrected

259   for spectral inter-element interferences (Table S1).

260

261   *2.8 Powder X-ray Diffraction*

262   The mineralogical composition of four samples, three from core A-11 at 7, 45 and

263   93 cm and 1 of bedrock from Nirp'pa Co's watershed, were analyzed using powder X-ray

264   diffraction. The XRD analyses were conducted using a Bruker D8 Discover instrument,

265   equipped with an IÁS Cu microsource of 1.54 Angstrom wavelength which provided an

266   X-ray beam through a 2mm point collimator. The X-ray diffraction pattern was detected

267   by a Lynxeye 1D detector. The X-ray source's operating conditions were voltage of 50

268   kV, and current of 1000uA. Qualitative mineral phase identification was performed using

269   Bruker's Diffrac.EVA software and the Crystallographic Open Database (COD; Table

270   S2).

271

272   *2.9 Sediment age*

273   Surface sediments from core A-11 were dated using ^{210}Pb, ^{214}Pb and ^{137}Cs

274 measured by direct gamma counting on 10 samples from the upper 9.5 cm (Table 1;

275 Appleby and Oldfield, 1983; Schelske et al., 1994). Radiocarbon ages from A-11 (n = 2)

276 and B -15 (n = 2) were determined by accelerator mass spectrometry (AMS ^{14}C) at the

277 University of California, Irvine (UCI), Keck AMS Facility on samples consisting of

278 charcoalized grass fragments, which were isolated by wet sieving sediment at 63 μm

279 (Table 2). The samples were manually cleaned and chemically pretreated with an acid-

280 alkali-acid wash of 1N HCl and 1N NaOH following UCI protocols. Radiocarbon ages

281 were calibrated with the online program CALIB 6.0 (Stuiver and Reimer, 1993) using the

282 IntCal 09.14c data set. We report the median probability age and 2σ error as thousands of

283 calendar years (ka) before present (B.P.; present = AD 1950).

284   [Insert Table 1]

285   [Insert Table 2]

286 **3. Results**

287 *3.1 Lithology*

288   Surface core A-11 is characterized by reddish brown fine-grained sediment that

289 becomes progressively darker reddish brown with depth. Banding was noted in the upper

290 30 cm and below 60 cm. Scattered organic fragments, including grass and charcoal are

291 visible throughout the core. Sediments in surface core A-15 were dark to medium gray

292 with no apparent banding. In surface core B-15, sediments were gray and coarse grained

293 with some banding distinguished by zones of increased organic matter from 94 to 74 cm.

294 Macroscopic charcoal and organic matter were particularly visible from 94 to 81 cm.

295 From 74 to 65 cm, B-15 sediments transition to a tan color with a darker brown band of

296   mottled sediment between 69 and 65 cm. From 65 to 44 cm, sediments are tan and fine

297   grained with some banding and still visible, but fewer organic particles. At 44 cm,

298   macroscopic organic matter particles increased until 5 cm. Above 5 cm, the sediments are

299   more olive green and the abundance of macroscopic plant fragments decreases.

300

301   *3.2 Chronology*

302   Excess ^{210}Pb (^{210}Pb$_{ex}$) activities were highest in core A-11 between 0 and 3.5 cm.

303   Below this depth, ^{210}Pb$_{ex}$ decays until reaching background activities at 7.5 cm. Using the

304   constant rate of supply model (CRS; Appleby and Oldfield, 1983), an age model was

305   constructed for the upper most sediment depths between 0 and 7.5 cm (Fig. 3). One

306   sample at 4.25 ± 0.25 cm contained measurable ^{137}Cs activities. Based on the ^{210}Pb CRS

307   age model, this sample dates to 1950-60 ± 4 CE. Samples above and below this, which

308   are dated at 1969-77and 1929-40 CE, respectively, contain no measurable ^{137}Cs.

309   Although slightly predating the 1963 CE ^{137}Cs maximum, the 4.25 cm sample's age is

310   within error of 1963 CE and consistent with the period during which atmospheric tests of

311   nuclear weapons were being conducted, supporting the ^{210}Pb CRS age model. Below 7.5

312   cm, two AMS ^{14}C ages of charcoalized grass fragments anchor the core chronology. A

313   second order polynomial was fit to the combined ^{210}Pb and AMS ^{14}C ages to

314   quantitatively establish the age-depth relationship, which spans the last 3.4 ka.

315   The polynomial age model uncertainty was evaluated by comparison with an age

316   model derived using the Bchron age modeling software (Blaauw and Christen, 2011: Fig.

317   S1). The polynomial age model is well within the 2-sigma confidence interval of the

318   Bchron age model while a regression between the two age models yielded a slope of 1.01

319 and an r^2 of 0.998. The Bchron age model, however, produces abrupt changes in

320 sedimentation rates at the ^{14}C age control points that are unlikely to reflect actual

321 sedimentation rate changes. For this reason, we utilize the polynomial age model, which

322 estimates more gradual changes in sedimentation rates.

323   The basal AMS ^{14}C sample for core B-15 at 90 cm returned an age of 11.25 ka

324 with the 66 cm sample returning an age of 4.5 ka (Table 1).

325   [Insert Figure 3]

326 *3.3 Bulk density, loss on ignition and the elemental and isotopic composition of organic*

327 *matter carbon and nitrogen*

328   Dry bulk density for core A-11 averaged 0.28 g cm^{-3} during the last 3.3 ka with

329 near average densities from 3.3 to 1.2 ka, above average densities between 1.2 ka and 60

330 cal yr B.P. and then a marked decrease to the present (Fig. 4a). Mass accumulation rates

331 averaged 8.7 x 10^{-3} g cm^{-2} yr^{-1} with a maximum of 15.9 x 10^{-3} g cm^{-2} yr^{-1} and a minimum

332 of 4.6 x 10^{-3} g cm^{-2} yr^{-1} and shows a similar trend with slowly increasing rates from 3.3 to

333 1.2 ka, a steeper increase between 1.2 ka and 60 cal yr B.P. and a sharp drop off to the

334 present (Fig. 4b).

335   [Insert Figure 4]

336   Organic matter abundances averaged 13.3 % and are characterized by a

337 decreasing trend from 3.3 ka to 360 cal yr B.P. that is marked by variations of up to ± 4

338 %. After 360 cal yr B.P., % OM increased sharply to the present (Fig. 4c). When

339 considered as flux, organic matter deposition averaged 1.1 x 10^{-3} g cm^{-2} yr^{-1} with a

340 maximum of 1.9 x 10^{-3} g cm^{-2} yr^{-1} and a minimum of 0.6 x 10^{-3} g cm^{-2} yr^{-1} and an

341 increasing trend that is similar to that of mass accumulation (Fig. 4d). Average carbonate

342   content was less than 3 %; variations in % TC most likely represent the loss of interstitial

343   water from clays.

344   The atomic ratio of carbon to nitrogen (C:N) averaged 11.1 during the last 3.3 ka

345   with a steady decreasing trend to the present, although with variability ranging between

346   14.5 and 9.4 (Fig. 4e). Biogenic silica concentrations averaged 10.8 % with values

347   ranging between 15.0 and 6.7 % (Fig. 4f). A slight decreasing trend is apparent over the

348   length of the record, but with considerable variability. When plotted as flux, a generally

349   increasing trend similar to organic matter flux is observed (Fig. 4). Organic matter $\delta^{13}C$

350   ($\delta^{13}C_{org}$) was relatively constant during the last 3.3 ka, varying by less than 1 ‰ about a

351   mean of -24.6 ‰ until 80 cal yr B.P., when $\delta^{13}C_{org}$ decreased to -25.9 ‰ (Fig. 4g). The

352   isotopic composition of sedimentary nitrogen averaged 2.6 ‰ and ranges from 3.1 to 2.1

353   ‰ (Fig. 4h). The data suggest a generally increasing trend towards present, with highest

354   values after 500 cal yr B.P.

355

356   *3.4 Lithics and Grain Size*

357   Down core lithic abundances in the Nir'pa Co record varied between 70.5 and

358   81.0 % with an average of 75.0 % (Fig. 5a). Correlations were positive with Ti (r = 0.70;

359   p < 0.001) and dry bulk density (r = 0.38; p = 0.096), null with % BSi and negative with

360   % TOM (r = -0.71; p < 0.001) as expected since % lithics was calculated from %TOM.

361   Still the lithics-TOM correlation is not 1:1, suggesting there is some signal captured. The

362   relationship between lithics and dry bulk density improves greatly (r = 0.64; p < 0.001) if

363   the most recent 110 years are excluded from the regression, which may reflect the

364   approximate time for flocculent sediment compaction to occur. Between 3.3 and 2.4 ka,

365 % lithics was near average at 74.1 % with low values between 3.3 and 2.9 ka and a peak

366 between 2.9 and 2.4 ka. At 2.4 ka % lithics decreased to an average of 73.8 % until 1.3

367 ka, but with variability. After 1.3 ka, % lithics increased to 77.3 %, but again with

368 variability. Peaks in % lithics occurred at 0.9, 0.4 and 0.1 ka with intervening drops. The

369 flux of lithic materials shows variations similar to % lithics, but with less variability prior

370 to 1.3 ka. From 3.3 to 1.3 ka, values generally increased, ranging between 2.2 and 10.1 x

371 10^{-3} g cm^{-2} yr^{-1} about a mean of 5.7 x 10^{-3} g cm^{-2} yr^{-1}. After 1.3 ka, lithic flux increased

372 more steeply plateauing at an average of 8.4 x 10^{-3} g cm^{-2} yr^{-1} by 950 cal yr B.P. (Fig.

373 5a). At 110 cal yr B.P., lithic flux began to decrease steeply to the present value of 6.1 x

374 10^{-3} g cm^{-2} yr^{-1}.

375   [Insert Figure 5]

376   The grain size distribution of the lithic fraction is dominated by silt, which varies

377 between 63.3 and 81.1 % and averages 71.5 % (Fig. 5b). Between 3.3 and 2.4 ka, % silt

378 was 2.4 % below the mean, averaging 69 %, before decreasing by a further 1 % to 68 %

379 between 2.4 and 1.4 ka (Fig. 5b, d). At 1.4 ka, % silt began a sustain increase to the

380 present, increasing by 6 % to 73.8 % . Clay is the next most abundant grain size fraction,

381 accounting for 27.6 % of the lithic component on average with a range between 18.6 and

382 36.5 % (Fig. 5e). Clay and silt are strongly anti-correlated at a near 1:1 relationship (m =

383 -1.01; r^2 = 0.88) over the duration of the record. Sand is the least abundant lithic

384 constituent, averaging just 1.5 %, but ranging of between 0.0 and 5.6 % (Fig. 5c).

385 Variations in % sand are distinct from those of silt and clay, but with transitions between

386 higher and lower concentrations coinciding with transitions in silt and clay. Between 3.3

387 and 2.4 ka and again between 1.4 ka and the present, % sand was generally low,

388   averaging 1.1 and 1.0 %, respectively. From 2.4 to 1.4 ka, % sand increased sharply,

389   averaging 3 % and reaching a maximum of 5.6 %.

390   Surface grab samples show consistent relationships between grain size, depth and

391   distance along the sampling transect (Fig. 2). As expected, % sand is highest in littoral

392   region closest to the ephemeral inlet with peak values of 58 %. Sand abundance

393   decreased away from the inlet toward the middle of the lake with sand in profundal sites

394   decreasing from 7 % to less than 1% at the A-11 core site. Silt and clay abundances are

395   lowest in the littoral zone and increase toward the center of the lake. Within the profundal

396   zone, % silt and % clay are largely consistent across the transect, but with a subtle

397   antiphased relationship.

398

399   *3.5 Analytical and XRF Ti abundances*

400   Geochemical analysis of the Nir'pa Co and Paru Co bedrock samples returned

401   high Ti values of 2360 and 2460 ppm, respectively. Ti concentrations in the glacial till

402   were similarly high, measuring 2290 ppm. Consistent with the sediment source

403   geochemisty (i.e., bedrock and till samples), XRF derived Ti in the Nir'pa Co sediment

404   core was high, averaging 7190 cps between a range of 10,510 and 5460 cps (Fig. 5g).

405   Values of Ti were below average, but with variability, between 3.3 and 1.2 ka, after

406   which time they increased to the top of the core. Both the long term and higher frequency

407   Ti variability closely resemble % lithics variations ($r = 0.70$; $p < 0.001$).

408

409   *3.6 X-ray diffraction mineralogy*

410   X-ray diffraction patterns from the bedrock sample indicate the presence of

411   quartz, feldspars, muscovite and titanite, consistent with its mapped andesitic

412   composition. Accordingly, the down core sediment samples from Nir'pa Co A-11 reflect

413   this bedrock mineralogy, showing similar assemblages (mainly quarts, feldspar,

414   muscovite and titanite) with the addition of clay weathering products (Table S1).

415

416   *3.7 Magnetic susceptibility*

417   Magnetic susceptibilities for core A-11 averaged 10.1 during the record with a

418   maximum of 17.5 and a minimum of 2.5 (Fig. 5f). Values were generally low between

419   3.3 and 1.5 ka with the exception of a broad peak between 2.8 and 2.4 ka. After 1.5 ka,

420   MS increased, but with superimposed centennial-scale variability at resembles that of the

421   Si/Ti ratio noted above. For A-15, MS averaged 11.0 with a maximum of 16.1 and a

422   minimum of 6.0. Trends similar to A-11 are noted in the A-15 MS with generally

423   increasing values with decreasing depth and peaks from 70 to 75 cm, 45 to 51 cm, 31 and

424   38 cm, and 10 to 21 cm (supplemental material). Although the magnitude of the peaks in

425   MS vary somewhat between the two cores, the correspondence is generally good

426   considering that A-11 was collected from near the middle of the lake and A-15 was

427   collected closer to the shore where the profundal zone begins to slope up toward the

428   shore.

429

430   **4. Discussion**

431   We focus on results from A-11 because its profundal location is less likely to be

432   affected by internal lake processes, such as near shore currents, which could affect

433   sediment characteristics (i.e., the location of A-15). Similarities between A-11 and A-15,

434   however, support generally consistent sedimentation across the lake basin, which give us

435   confidence that the A-11 results are representative of the lake's hydroclimate variations

436   during the late Holocene (Fig. S3). Core B-15 is not included in the discussion because

437   the initial ^{14}C results indicate that it likely contains hiatuses and is not a complete record

438   of Holocene climate. Nonetheless, the basal age of 11.25 ka is consistent with the basal

439   age from nearby Paru Co, suggesting that lakes in the region deglaciated and filled

440   rapidly at this time.

441

442   *4.1 Lithic and grain size proxy interpretation*

443   Grain size measurements of lacustrine sediments offer insight into watershed and

444   in lake processes that are sensitive to climatic variations (e.g., Shuman et al., 2009;

445   Dearing, 1997; Conroy et al., 2008). Today at Nir'pa Co, below freezing temperatures

446   and minimal precipitation between November and April limit watershed erosion and the

447   transport of clastic material to the lake during the cold season (Fig. 2c). At the same time,

448   cold season ice cover precludes sediment influx to Nir'pa Co while also limiting

449   autochthonous biological productivity. As such, sediment deposition at the lake is largely

450   restricted to the warm summer months when clastic material can be mobilized by

451   monsoonal precipitation after above freezing temperatures removes snow cover from the

452   watershed and ice cover from the lake. Watershed and in-lake productivity also increase

453   during this time, although the degree of productivity is controlled by multiple factors,

454   including average temperature, precipitation, pH, nutrient availability and turbidity

455   (Carpenter et al., 1985; Catalan et al., 2009).

456   Given the highly seasonal climate at Nir'pa Co and the regional dominance of the

457   ISM on the summer hydrologic regime, we interpret Nir'pa Co's clastic sediment record

458   as reflecting watershed and depositional processes that are linked to summer climatic

459   conditions associated with the ISM. The lithic fraction, which averages more than half of

460   the sediment total, is by far the dominant component of Nir'pa Co's sediment archive

461   record. Of this component, silt is the primary grain size fraction, averaging 72.9 %

462   followed by % clay and % sand. Modern grain size distributions show that silt and clay

463   are relatively evenly distributed across Nir'pa Co's profundal zone, although with an

464   antiphased relationship (Fig. 2). Increases in one constituent, therefore, necessarily lead

465   to the reduction of the other. We suggest that the down core antiphased relationship

466   between % silt and % clay reflects variations in runoff intensity, such that silt (clay)

467   content would increase (decrease) when runoff intensity was enhanced (diminished), and

468   vice versa. This is supported by the similarities between % silt and % lithics ($r = 0.51$, $p <$

469   0.001), which are interpreted as the relative contribution of clastic material delivered to

470   the lake (Sly, 1978). We suggest % lithics is primarily controlled by summer

471   precipitation whereby enhanced rainfall results in greater lithic mobilization in the

472   watershed. At the same time, % silt abundances reflect increased runoff energy during

473   times of greater lithic influx.

474   Down core variations in % sand are distinct from those in lithics, silt and clay, but

475   with transitions that were contemporaneous with changes in silt, clay and lithics (Fig. 5).

476   This suggests that different, but still climatically related processes resulted in changes in

477   the proportion of sand deposited at the core site. Today, sand abundance is clearly linked

478   to lake levels with minimum sand in profundal sites and increasing abundances toward

479   the littoral and inlet regions. Because much of Nir'pa Co's bathymetry is steep sided with

480   a flat bottom, changes in lake level will not greatly increase the proximity of the littoral

481   zone for most of the lake's basin (Håkanson, 1982). At the lake's shallow north end,

482   however, small changes in lake level will more significantly reduce the distance between

483   the core site and the point at which seasonal fluvial discharge enters the lake. For

484   example, a lake level decrease of ~1.5 m would increase the proximity of fluvial inputs

485   and the core site by approximately 130 m (Fig. 2b). Although encroachment of the littoral

486   zone at other points around the lake basin might also be important, the net result of

487   increased sand with lower lake levels would remain consistent. We therefore interpret %

488   sand as a lake level indicator such that increased sandiness reflects lower lake levels with

489   more proximal fluvial discharge and reduced sandiness reflects higher lake levels and

490   more distal fluvial discharge relative to the core site. That sand increased during times

491   when % silt and lithics decreased, is consistent with our interpretation because if

492   increased sandiness were related to depositional energy, we would expect it to increase in

493   phase with % silt and lithics, not decrease as is observed.

494

495   *4.2 Magnetic susceptibility and Si/Ti*

496   The magnetic susceptibility and Ti abundance in lacustrine sediments have been

497   widely used as indicators of the contribution of terrestrial clastic material (Seltzer et al.,

498   2002; Metcalfe et al., 2010). At Nir'pa Co, MS and Ti closely track changes in % lithics

499   and silt, although with important differences, particularly after 1.3 ka, generally

500   supporting the hypothesis of terrestrial erosion control. Subtle differences between Ti and

501   MS, however, indicate that processes other than terrestrial input may be reflected in the

502   MS profile.

503   [Insert Figure 6]

504   *4.3 Late Holocene ISM rainfall at Nir'pa Co*

505   Based on the sedimentological characteristics of Nir'pa Co's clastic sediment

506   fraction, we identified three distinct multi-century-scale phases of hydroclimate

507   variability during the last 3.3 ka within a larger trend of generally increasing precipitation

508   (Fig. 6). Two periods of elevated lithic and silt abundance with low clay and sand content

509   occurred between 3.3 and 2.4 ka and 1.3 ka and the present, suggesting wetter conditions

510   and a strengthened ISM. Although MS does not show a strong increase during the earliest

511   inferred wet period between 3.3 and 2.4 ka, it does increase significantly after 1.3 ka in

512   step with lithics, % silt and Ti, indicating that the increase in ISM precipitation was large

513   enough to register in all proxies. The intervening period from 2.4 to 1.3 ka, with its lower

514   silt and lithic content, but elevated sand and clay content, suggests drier conditions with

515   lower lake levels.

516   Superimposed on these millennial-scale ISM variations were higher frequency

517   century-scale ISM variations; however, these are comparatively minor when considered

518   within the context of the lower frequency variations (Fig 6). In particular, it is notable

519   that relatively minor sedimentological responses are apparent at Nir'pa Co during the

520   MCA (950 to 800 cal yr B.P.). Although subtle and not statistically significant (two-

521   sample t-test null hypothesis not rejected), decreasing sand and elevated silt and lithics

522   during the MCA may possibly reflect an increase in ISM rainfall that resulted in higher

523   lake levels and greater watershed erosion during this event (Fig. 6a-c). Increasing % sand

524   and slightly reduced lithics and % silt during the LIA from 500 to 200 cal yr B.P. may

525   suggest a drier LIA at Nir'pa Co. It is important to stress, however, that sedimentological

526   responses during the MCA and LIA were minor compared to the millennial scale increase

527   in ISM precipitation on which they are superimposed and that additional records with

528   greater temporal resolution and climatic sensitivity are needed to more robustly

529   investigate MCA and LIA hydroclimate expressions in this region.

530

531   *4.4 Late Holocene productivity at Nir'pa Co*

532   Paleo productivity at Nir'pa Co is interpreted from several indicators, including %

533   OM, OM flux, the elemental abundance and isotopic composition of organic carbon and

534   sedimentary nitrogen, and biogenic silica.

535   The decreasing trend in % OM at Nir'pa Co from 3.3 ka to 360 cal yr B.P., is

536   attributed to dilution from increasing clastic sedimentation as indicated by greater lithic

537   composition and mass accumulation rates, particularly after 1.3 ka (Fig. 4 & 5). When

538   considered as flux, OM shows an increasing trend during the late Holocene that is anti-

539   phased with decreasing C:N, implicating enhanced aquatic productivity as the cause of

540   this trend (Fig. 5). Biogenic silica also shows an increasing trend when considered as

541   flux, additionally supporting the idea that aquatic productivity increased through the late

542   Holocene. At the same time, $\delta^{13}C_{org}$ varies by less then 1 ‰, with the exception of one

543   surface sample that was markedly more negative than the late Holocene average,

544   suggesting that aquatic productivity was the source of sedimentary organic matter and

545   that only its production intensity changed through time.

546

547   *4.5 Late Holocene ISM variability on the Third Pole*

548   Despite generally more arid late Holocene conditions (Gasse et al., 1996; Bird et

549   al., 2014; Cai et al., 2012; Zhu et al., 2008; Mügler et al., 2010), comparison of Nir'pa Co

550   results with other Third Pole paleoclimate records indicates periods of coherent

551   hydroclimatic variability on the central and eastern Tibetan Plateau (Fig. 6). At nearby

552   Paru Co, for example, reconstructed lake levels were higher between 3.3 and 2.5 ka and

553   1.3 ka and the present, with an intervening period of declining lake level between 2.4 and

554   1.3 ka (Fig 6d). Erosion at Paru Co was also significantly enhanced after 1.3 ka,

555   consistent with trends at Nir'pa Co (Fig. 6e). Although low resolution, the hydrogen

556   isotopic composition of leaf wax n-alkanes (δD_{wax}) at Paru Co broadly suggests similar

557   late Holocene hydrologic variability with lower δD_{wax} corresponding to periods of

558   increased precipitation, erosion and high lake levels and higher δD_{wax} corresponding to

559   periods of reduced ISM precipitation, reduced erosion and lower lake levels at Paru Co

560   and Nir'pa Co (Fig. 6f).

561   At Seling Co, the largest lake in Tibet and located approximately 370 km

562   northwest of Nir'pa Co, late Holocene $\delta^{18}O_{cal}$ values were relatively low from 3.3 to 2.4

563   ka and after 1.4 ka, suggesting wetter conditions during these times (Fig. 6f; Gu et al.,

564   1993). Between 2.4 and 1.4 ka, higher $\delta^{18}O_{cal}$ at Seling Co suggests enhanced aridity.

565   Similar trends are noted in grain size, mineralogical and geochemical proxies at Nam Co,

566   the second largest lake on the Tibetan Plateau, which is approximately 180 km northwest

567   of Nir'pa Co (Mügler et al., 2010; Zhu et al., 2008). A generally stable environment is

568   suggested for Nam Co between 4 and 1.6 ka with a marked period of aridity between 1.6

569   and 1.4 ka. After 1.4 ka, wetter conditions persisted until 800 cal yr B.P., after which

570 point aridity was again inferred. Considered as a whole, the similar trends at Seling Co

571 and Nam, Nir'pa Co and Paru Co, particularly since 1.4 ka, suggest regionally similar

572 multi-centennial to millennial-scale hydroclimate on the southeastern and central Tibetan

573 Plateau.

574 The hydroclimatic variations inferred from Tibetan lake sediment records are

575 generally similar with inferred changes in surface air temperatures as reconstructed with a

576 pollen biome index technique applied to results from Lake Zigetang (Fig. 6i; Herzschuh

577 et al., 2006). Elevated air temperatures are suggested to have persisted between 3.3 and

578 2.3 ka and after 1.4 ka with cooler air temperatures between 2.3 and 1.4 ka. This suggests

579 that increased ISM precipitation between 3.3 and 2.4 ka and 1.3 ka and the present was

580 broadly associated with warmth on the Tibetan Plateau whereas reduced ISM rainfall

581 between 2.4 and 1.3 ka coincided with cooler air temperatures. This pattern was also

582 noted for other lake high stands and precipitation increases during the middle and early

583 Holocene at Paru Co (Bird et al., 2014).

584 In contrast with the largely similar expression of ISM variability on central and

585 eastern Tibetan Plateau, the Bangong Lake δ^{18}O record from western Tibet shows

586 different trends during the last 3 ka (Fig. 6h; Gasse et al., 1996). Increasing δ^{18}O after 3.3

587 ka is interrupted at 2.4 ka by a period of steady to lower δ^{18}O that lasted until 1.3 ka.

588 After 1.3 ka, δ^{18}O at Bangong Lake increased abruptly to maximum late Holocene values

589 that then decrease slowly. It is possible that the Bangong Lake δ^{18}O data reflects regional

590 changes in effective moisture, with the last 1.3 ka being a period of considerably higher

591 evaporation and reduced ISM precipitation that did not penetrate into western Tibet. This

592 idea is consistent with recent work that showed lakes levels in western Tibet were more

593 sensitive to long-term reductions in ISM precipitation than those in the east, which are

594 closer to the source of ISM moisture (Hudson and Quade, 2013). It is also possible that

595 moisture from the mid-latitude westerlies, which has elevated $\delta^{18}O$ relative to monsoonal

596 precipitation (Tian et al., 2007), increased during this time as the ISM weakened.

597

598 *4.6 Regional late Holocene ISM expressions*

599   The ISM trends discussed above are also expressed in proxy records more distal

600 to the Tibetan Plateau, but still within the sphere of ISM influence. A foraminifera-based

601 upwelling record from the Arabian Sea, for example, shows enhanced upwelling,

602 suggesting a strengthened ISM during the two pluvial phases identified at Nir'pa Co

603 between 3.3 and 2.4 ka and 1.3 ka to the present with the latter stronger than the former

604 (Fig. 7e; Gupta et al., 2005; Overpeck et al., 1996). Between 2.4 and 1.5 ka, upwelling is

605 reduced relative to the preceding and following periods. The Oman speleothem $\delta^{18}O$

606 record, which has been interpreted as reflecting the northerly (wet) or southerly (dry)

607 position of the Intertropical Convergence Zone (ITCZ), shows relatively little $\delta^{18}O$

608 variability, but contains a hiatus between 2.7 and 1.4 ka (Fig. 7f). This may suggests that

609 reduced precipitation during this time, possibly reflecting a southerly mean position of

610 the ITCZ, precluded drip water percolation and calcite formation (Fleitmann et al., 2007).

611   [Insert Figure 7]

612   Although temporally limited, trends in a 900-yr-long $\delta^{18}O$ record from Dendak

613 Cave, India, show some similarities with the Third Pole records (Fig. 6j; Sinha et al.,

614 2006). The initiation of calcite precipitation at Dandak Cave at approximately 1.3 ka

615 coincides with the end of the arid interval at Nir'pa Co between 2.4 and 1.3 ka. This may

616   indicate that a shift to increased precipitation at Dandak Cave at time permitted calcite to

617   form. Generally low $\delta^{18}O$ between 1020 and 690 cal yr B.P., suggests an interval of

618   enhanced ISM precipitation that coincides with the MCA. This is consistent with another

619   speleothem from Sahiya Cave (30º 36'N, 77º 52'E, 1190 m asl) that shows low $\delta^{18}O$

620   during the MCA between 1050 and 650 cal yr B.P., indicating enhanced ISM

621   precipitation and moisture delivery from the Bay of Bengal (Sinha et al., 2015). This

622   supports the tentative evidence from Nir'pa Co that the MCA may have been a period of

623   slightly greater ISM precipitation on the central/eastern Tibetan Plateau. Increasing $\delta^{18}O$

624   after 650 and 690 cal yr B.P, in the Dandak and Sahiya Cave records, respectively,

625   although with variability, and the cession of calcite precipitation at 390 cal yr B.P. at

626   Dandack cave, suggest a shift to increasing aridity during the LIA that coincides with

627   potentially drier conditions at Nir'pa Co. It is important to stress, however, that the MCA

628   and LIA signals in the Nir'pa Co record are not statistically significant, which suggests

629   that these events were not strongly expressed in at least the southeastern portion of the

630   Tibetan Plateau. Additional records are needed from this and other regions across Tibet in

631   order to better evaluate the expression of these events and whether or not they were

632   indeed climatically significant intervals.

633

634   *4.7 Mechanisms of late Holocene ISM precipitation trends*

635   The largely coherent multi-centennial ISM trends noted in lake sediment records

636   from the central and eastern Tibetan Plateau suggest common, large-scale forcing

637   mechanisms. Although some work suggests that the modern ENSO-ISM relationship was

638   only established during the last 2000 years, previous work investigating Holocene ISM

639   on the Third Pole showed that it closely followed Indo-Pacific sea surface temperatures

640   (SST) and ENSO-like ocean-atmosphere variability on centennial and millennial scales

641   through the Holocene (Bird et al., 2014). Comparison of the Nir'pa Co results and other

642   Third Pole records shows that periods of inferred wet conditions between 3.3 and 2.4 ka

643   and from 1.3 ka and the present similarly coincided with Indo-Pacific warming and

644   eastern equatorial Pacific cooling suggestive of La Niña-like conditions (Fig. 7h & i;

645   Koutavas et al., 2006; Marchitto et al., 2010). Although SST reconstructions spanning the

646   last 2 ka are not available from the EEP, an El Niño record from El Junco, a crater lake in

647   the Galapagos Islands, provides supporting evidence for late Holocene ENSO variability

648   that is consistent with SST records from the Indo-Pacific (Fig. 7g; Conroy et al., 2008).

649   Generally low % sand in the El Junco record from 3.3 to 2.4 ka and 1.3 ka to the present

650   is interpreted to reflect reduced precipitation over the lake's watershed, which occurs

651   today during La Niña conditions. Persistent La Niña-like conditions from 3.3 to 2.4 ka

652   and 1.3 ka to the present is consistent with the Nir'pa Co results and other Third Pole

653   records, which suggest wetter and warmer conditions during these times. Peak % sand at

654   El Junco between 2.4 and 1.3 ka, suggesting persistent El Niño-like conditions, coincides

655   with lake level decreases at Nir'pa Co and Paru Co, aridity at Seling Co and Nam Co and

656   cooling on the Tibetan Plateau. The suggested occurrence of El Niño-like conditions

657   between 2.4 and 1.3 ka is consistent with Indo-Pacific cooling and the modern

658   relationship between El Niño, reduced ISM precipitation and cooling as a result of

659   enhanced Tibetan Plateau snow pack (Shaman and Tziperman, 2005). Similar ENSO

660   patterns are observed at Laguna Pallcacocha, Ecuador, with the exception of the period

661   between 2.4 and 1.7 ka, when fewer than 5 ENSO events per century were observed and

662   the El Junco record suggests enhanced El Niño-like conditions (Moy et al., 2002). The El

663   Junco record, however, may better reflect EEP ENSO-like variability because its location

664   in the Galapagos Islands is more directly linked to Pacific SST and convective activity

665   (Conroy et al., 2008).

666   The relatively minor expressions of the MCA and LIA in the higher resolution

667   record from Nir'pa Co suggests that lower-frequency climate processes, particularly

668   those acting in the Indo-Pacific, may have been more fundamental in determining the

669   mean state of the late Holocene ISM. Still, that the ISM appears to have strengthened

670   during the MCA and weakened during the LIA is consistent with evidence for La Niña-

671   like and El Niño-like conditions during these events, respectively (Mann et al., 2009).

672

673   **5. Summary and Conclusions**

674   The Nir'pa Co sediment record provides a detailed view of late Holocene ISM

675   variability from the southeastern Tibetan Plateau spanning the last 3.3 ka. Within the

676   context a generally weakened late Holocene ISM, two pluvial phases are identified. The

677   strongest pluvial phase, which is recognized in other records from the central and eastern

678   Tibetan Plateau occurred between 1.3 ka and the present. A second, less intense, pluvial

679   phase occurred between 3.3 and 2.4 ka.

680   Between these pluvial phases, a pronounced arid interval occurred between 2.4

681   and 1.3 ka. Other paleoclimate records from the Third Pole also indicate aridity during

682   this time, suggesting that this was a widespread event. The two pluvial phases occurred in

683   conjunction with warmer surface air temperatures on the Tibetan Plateau, elevated SST in

684   the Indo-Pacific and lower SST in the EEP. These conditions are consistent with a La

685   Niña-like mean state in the tropical Pacific, suggesting that Indo-Pacific ocean-

686   atmosphere variability contributed to these events. This idea is supported by a lake

687   sediment record from El Junco in the ENSO-sensitive Galapagos Islands, which suggests

688   La Niña-like conditions occurred during inferred pluvial phases at Nir'pa Co.

689   Conversely, aridity at Nir'pa Co between 2.4 and 1.3 ka occurred in conjunction with

690   reduced Indo-Pacific SST and cooling on the Tibetan Plateau, which are suggestive of

691   enhanced El Niño-like conditions. The El Junco record again supports this idea, showing

692   the greatest increase in % sand during the late Holocene, which has been interpreted as

693   reflecting enhanced El Niño conditions. These associations between variations in ISM

694   precipitation, Tibetan Plateau surface air temperatures and Pacific ocean atmosphere

695   variability are consistent with modern relationships observed in the instrumental record

696   whereby El Niño/El Niño-like conditions produce reductions in ISM precipitation and La

697   Niña/La Niña-like conditions enhance the ISM.

698   Although the above ISM phases are noted in multiple records from the Third Pole,

699   the Bangong Co record from western Tibet shows opposite trends during the late

700   Holocene. This suggests that ISM variability during the last 3 ka differed across the

701   Tibetan Plateau. This may reflect the inability of the ISM to exert a strong influence

702   across the Tibetan Plateau as a result of its generally weakened mean state during the late

703   Holocene. As a result, evaporation in western Tibet may have increased with little

704   moderation by the two pluvial events noted in the central and eastern Tibetan Plateau.

705   This is consistent with and east-west asymmetry in Holocene lake level trends that show

706   greater evaporation sensitivity in western Tibet. The last 1000 years may also have

707   experienced increased moisture from westerly sources as a result of strengthened

708   westerlies that delivered isotopically lighter precipitation.

709   Superimposed on the millennial-scale ISM variations noted above were minor

710   higher frequency, but lower amplitude changes in ISM precipitation. Although subtle and

711   not statistically significant, possible increases in ISM rainfall and lake levels occurred

712   during the MCA while reductions in ISM rainfall and lower lake levels are suggested for

713   the LIA. These hydroclimate expressions of the MCA and LIA are consistent with

714   regional evidence from speleothems and recent work combining proxy records and

715   climate model simulations suggesting a La Niña-like mean state in Pacific ocean-

716   atmosphere system during the MCA and an El Niño-like mean state during the LIA.

717   Additional records with improved spatial and temporal resolution are needed, however, to

718   better assess the apparently subtle expressions of the MCA and LIA in the ISM region.

719   The patterns and mechanisms of late Holocene ISM variability identified in the

720   Nir'pa Co and other Third Pole records are consistent with those identified for the early

721   and middle Holocene (e.g. Bird et al., 2014). This suggests that the tropical Pacific's

722   response to warming (Clement et al., 1996; Marchitto et al., 2010; England et al., 2014)

723   to warming may continue to enhance ISM precipitation on the Tibetan Plateau, as has

724   been apparent from the expansion of lakes across the plateau, but particularly in the

725   central and eastern sections over the last few decades (Lei et al., 2013). Additional and

726   higher-resolution records are needed from the Third Pole region, however, in order to

727   confirm our findings, evaluate their spatiotemporal coherence, and investigate additional

728   controls on multi-decadal ISM rainfall through the Holocene (e.g., solar and Atlantic

729   Ocean-atmosphere variability).

730

Data

All original data presented in this paper are publically available via the NOAA

Paleoclimate Database (a url to the data will be included in the final manuscript pending

acceptance).

References

Appleby PG and Oldfield F. (1983) The assessment of ^{210}Pb data from sites with varying
    sedimentation accumulation rates. *Hydrobiologia* 103: 29-35.
Ashok K, Guan Z, Saji N, et al. (2004) Individual and combined influences of ENSO and
    the Indian Ocean dipole on the Indian summer monsoon. *Journal of Climate* 17:
    3141-3155.
Ashok K, Guan Z and Yamagata T. (2001) Impact of the Indian Ocean Dipole on the
    relationship between the Indian monsoon rainfall and ENSO. *Geophysical
    Research Letters* 28: 4499-4502.

757 Berkelhammer M, Sinha A, Stott L, et al. (2012) An abrupt shift in the Indian monsoon
758   4000 years ago. *Climates, Landscapes, and Civilizations*. Washington, DC: AGU,
759   75-87.
760 Bird BW, Abbott MB, Vuille M, et al. (2011) A 2300-year-long annually resolved record
761   of the South American summer monsoon from the Peruvian Andes. *Proceedings*
762   *of the National Academy of Sciences* 108: 8583-8588.
763 Bird BW, Polisar PJ, Lei Y, et al. (2014) A Tibetan lake sediment record of Holocene
764   Indian summer monsoon variability. *Earth and Planetary Science Letters* 399: 92-
765   102.
766 Blaauw M and Christen JA. (2011) Flexible paleoclimate age-depth models using an
767   autoregressive gamma process. *Baysian Analysis* 6: 457-474.
768 Cai Y, Zhang H, Cheng H, et al. (2012) The Holocene Indian monsoon variability over
769   the southern Tibetan Plateau and its teleconnections. *Earth and Planetary Science*
770   *Letters* 335-336: 135-144.
771 Carpenter SR, Kitchell JF and Hodgson JR. (1985) Cascading trophic interactions and
772   lake productivity. *BioScience*: 634-639.
773 Catalan J, Pla S, García J, et al. (2009) Climate and CO2 saturation in an alpine lake
774   throughout the Holocene. *Limnology and Oceanography* 54: 2542.
775 Chen J, Chen F, Feng S, et al. (2015) Hydroclimatic changes in China and surroundings
776   during the Medieval Climate Anomaly and Little Ice Age: spatial patterns and
777   possible mechanisms. *Quaternary Science Reviews* 107: 98-111.
778 Choubert G, Faure-Muret A and Chanteux P. (1983) *Atlas géologique du monde*: Unesco.
779 Clement AC, Seager R, Cane MA, et al. (1996) An ocean dynamical thermostat. *Journal*
780   *of Climate* 9: 2190-2196.
781 Conroy JL, Overpeck JT, Cole JE, et al. (2008) Holocene changes in eastern tropical
782   Pacific climate inferred from a Galápagos lake sediment record. *Quaternary*
783   *Science Reviews* 27: 1166-1180.
784 Dearing J. (1997) Sedimentary indicators of lake-level changes in the humid temperate
785   zone: a critical review. *Journal of Paleolimnology* 18: 1-14.
786 England MH, McGregor S, Spence P, et al. (2014) Recent intensification of wind-driven
787   circulation in the Pacific and the ongoing warming hiatus. *Nature Climate Change*
788   4: 222-227.
789 Fleitmann D, Burns SJ, Mangini A, et al. (2007) Holocene ITCZ and Indian monsoon
790   dynamics recorded in stalagmites from Oman and Yemen (Socotra). *Quaternary*
791   *Science Reviews* 26: 170-188.
792 Gadgil S. (2003) The Indian monsoon and its variability. *Annual Review of Earth and*
793   *Planetary Sciences* 31: 429-467.
794 Gasse F, Fontes JC, Van Campo E, et al. (1996) Holocene environmental changes in
795   Bangong Co basin (Western Tibet). Part 4: discussion and conclusions.
796   *Palaeogeography, Palaeoclimatology, Palaeoecology* 120: 79-92.
797 Goswami BN, Madhusoodanan MS, Neema CP, et al. (2006) A physical mechanism for
798   North Atlantic SST influence on the Indian summer monsoon. *Geophysical*
799   *Research Letters* 33: L02706.
800 Gray AB, Pasternack GB and Watson EB. (2010) Hydrogen peroxide treatment effects on
801   the particle size distribution of alluvial and marsh sediments. *The Holocene* 20:
802   293-301.

803   Gu Z, Liu J, Yuan B, et al. (1993) The changes in monsoon influence in the Qinghai-
804   Tibetan Plateau during the past 12,000 years. Geochemical evidence from the L.
805   Selin sediments. *Chinese Science Bulletin* 38: 61-64.
806   Gupta AK, Das M and Anderson DM. (2005) Solar influence on the Indian summer
807   monsoon during the Holocene. *Geophysical Research Letters* 32: L17703.
808   Håkanson L. (1982) Lake bottom dynamics and morphometry: The dynamic ratio. *Water*
809   *Resources Research* 18: 1444-1450.
810   He Y, Theakstone WH, Zhonglin Z, et al. (2004) Asynchronous Holocene climatic
811   change across China. *Quaternary Research* 61: 52-63.
812   Heiri O, Lotter AF and Lemcke G. (2001) Loss on ignition as a method for estimating
813   organic and carbonate content in sediments: reproducibility and comparability of
814   results. *Journal of Paleolimnology* 25: 101-110.
815   Herzschuh U, Winter K, Wünnemann B, et al. (2006) A general cooling trend on the
816   central Tibetan Plateau throughout the Holocene recorded by the Lake Zigetang
817   pollen spectra. *Quaternary International* 154-155: 113-121.
818   Hong YT, Hong B, Lin QH, et al. (2005) Inverse phase oscillations between the East
819   Asian and Indian Ocean summer monsoons during the last 12000 years and paleo-
820   El Niño. *Earth and Planetary Science Letters* 231: 337-346.
821   Hong YT, Hong B, Lin QH, et al. (2003) Correlation between Indian Ocean summer
822   monsoon and North Atlantic climate during the Holocene. *Earth and Planetary*
823   *Science Letters* 211: 371-380.
824   Hudson AM and Quade J. (2013) Long-term east-west asymmetry in monsoon rainfall on
825   the Tibetan Plateau. *Geology* 41: 351-354.
826   Koutavas A, Olive GC and Lynch-Stieglitz J. (2006) Mid-Holocene El Niño–Southern
827   Oscillation (ENSO) attenuation revealed by individual foraminifera in eastern
828   tropical Pacific sediments. *Geology* 34: 993-996.
829   Krishnamurthy V and Kirtman BP. (2009) Relation between Indian monsoon variability
830   and SST. *Journal of Climate* 22: 4437-4458.
831   Krishnan R and Sugi M. (2003) Pacific decadal oscillation and variability of the Indian
832   summer monsoon rainfall. *Climate Dynamics* 21: 233-242.
833   Kumar KK, Rajagopalan B, Hoerling M, et al. (2006) Unraveling the mystery of Indian
834   monsoon failure during El Niño. *Science* 314: 115-119.
835   Lawrimore JH, Menne MJ, Gleason BE, et al. (2011) An overview of the Global
836   Historical Climatology Network monthly mean temperature data set, version 3.
837   *Journal of Geophysical Research* 116: D19121.
838   Lei Y, Yao T, Bird BW, et al. (2013) Coherent lake growth on the central Tibetan Plateau
839   since the 1970s: Characterization and attribution. *Journal of Hydrology* 483: 61-
840   67.
841   Liu X, Dong H, Yang X, et al. (2009) Late Holocene forcing of the Asian winter and
842   summer monsoon as evidenced by proxy records from the northern Qinghai–
843   Tibetan Plateau. *Earth and Planetary Science Letters* 280: 276-284.
844   Mann ME, Zhang Z, Rutherford S, et al. (2009) Global signatures and dynamical origins
845   of the Little Ice Age and Medieval Climate Anomaly. *Science* 326: 1256-1260.
846   Marchitto TM, Muscheler R, Ortiz JD, et al. (2010) Dynamical response of the tropical
847   Pacific Ocean to solar forcing during the early Holocene. *Science* 330: 1378-
848   1381.

849 Metcalfe SE, Jones MD, Davies SJ, et al. (2010) Climate variability over the last two
850   millennia in the North American Monsoon region, recorded in laminated lake
851   sediments from Laguna de Juanacatlán, Mexico. *The Holocene*.
852 Mischke S and Zhang C. (2010) Holocene cold events on the Tibetan Plateau. *Global and*
853   *Planetary Change* 72: 155-163.
854 Morrill C, Overpeck JT and Cole JE. (2003) A synthesis of abrupt changes in the Asian
855   summer monsoon since the last deglaciation. *The Holocene* 13: 465-476.
856 Morrill C, Overpeck JT, Cole JE, et al. (2006) Holocene variations in the Asian monsoon
857   inferred from the geochemistry of lake sediments in central Tibet. *Quaternary*
858   *Research* 65: 232-243.
859 Mortlock RA and Froelich PN. (1989) A simple method for the rapid determination of
860   biogenic opal in pelagic marine sediments. *Deep Sea Research Part A.*
861   *Oceanographic Research Papers* 36: 1415-1426.
862 Moy CM, Seltzer GO, Rodbell DT, et al. (2002) Variability of El Nino/Southern
863   Oscillation at millennial timescales during the Holocene epoch. *Nature* 420: 162-
864   165.
865 Mügler I, Gleixner G, Günther F, et al. (2010) A multi-proxy approach to reconstruct
866   hydrological changes and Holocene climate development of Nam Co, Central
867   Tibet. *Journal of Paleolimnology* 43: 625-648.
868 Overpeck J, Anderson D, Trumbore S, et al. (1996) The southwest Indian Monsoon over
869   the last 18000 years. *Climate Dynamics* 12: 213-225.
870 Peings Y and Douville H. (2010) Influence of the Eurasian snow cover on the Indian
871   summer monsoon variability in observed climatologies and CMIP3 simulations.
872   *Climate Dynamics* 34: 643-660.
873 Peterson TC and Vose RS. (1997) An overview of the Global Historical Climatology
874   Network temperature database. *Bulletin of the American Meteorological Society*
875   78: 2837-2849.
876 Qiu J. (2008) The Third Pole. *Nature* 454: 393-396.
877 Schelske CL, Peplow A, Brenner M, et al. (1994) Low-background gamma counting:
878   applications for ^{210}Pb dating of sediments *Journal of Paleolimnology* 10: 115-128.
879 Seltzer GO, Rodbell DT, Baker PA, et al. (2002) Early Warming of Tropical South
880   America at the Last Glacial-Interglacial Transition. *Science* 296: 1685-1686.
881 Shaman J and Tziperman E. (2005) The effect of ENSO on Tibetan Plateau snow depth:
882   A stationary wave teleconnection mechanism and implications for the South
883   Asian monsoons. *Journal of Climate* 18: 2067-2079.
884 Shuman B, Henderson AK, Colman SM, et al. (2009) Holocene lake-level trends in the
885   Rocky Mountains, USA. *Quaternary Science Reviews* 28: 1861-1879.
886 Sinha A, Cannariato KG, Stott LD, et al. (2006) A 900-year (600 to 1500 A.D.) record of
887   the Indian summer monsoon precipitation from the core of the monsoon zone of
888   India. *Geophysical Research Letters* 34: L16707.
889 Sinha A, Kathayat G, Cheng H, et al. (2015) Trends and oscillations in the Indian
890   summer monsoon rainfall over the last two millennia. *Nature communications* 6.
891 Sly P. (1978) Sedimentary processes in lakes. *Lakes.* Springer, 65-89.
892 Stott L, Cannarlato K, Thunnell R, et al. (2004) Decline of surface temperature and
893   salinity in the western tropical Pacific Ocean in the Holocene epoch. *Nature* 431:
894   56-59.

895 Stuiver M and Reimer PJ. (1993) Extended ^{14}C database and revised CALIB radiocarbon
896   calibration program. *Radiocarbon* 35: 215-230.
897 Thompson LG, Yao T, Mosley-Thompson E, et al. (2000) A high-resolution millennial
898   record of the South Asian monsoon from Himalayan ice cores. *Science* 289: 1916-
899   1919.
900 Tian L, Masson-Delmotte V, Stievenard M, et al. (2001) Tibetan Plateau summer
901   monsoon northward extent revealed by measurements of water stable isotopes.
902   *Journal of Geophysical Research* 106: 28081-28088.
903 Tian L, Yao T, MacClune K, et al. (2007) Stable isotopic variations in west China: A
904   consideration of moisture sources. *Journal of Geophysical Research* 112:
905   D10112.
906 Yanhong W, Lücke A, Zhangdong J, et al. (2006) Holocene climate development on the
907   central Tibetan Plateau: A sedimentary record from Cuoe Lake.
908   *Palaeogeography, Palaeoclimatology, Palaeoecology* 234: 328-340.
909 Zhang P, Cheng H, Edwards RL, et al. (2008) A test of climate, sun and culture
910   relationships from an 1810-year Chinese cave record. *Science* 322: 940-942.
911 Zhu L, Wu Y, Wang J, et al. (2008) Environmental changes since 8.4 ka reflected in the
912   lacustrine core sediments from Nam Co, central Tibetan Plateau. *The Holocene*
913   18: 831-839.
914
915 **Figure Captions**

916 **Figure 1:** Map of the broader study region showing the location of paleoclimate sties

917 discussed in the test. Nir'pa Co is marked with a red circle. Other lakes records are

918 indicated with black circles. Cave records are identified with an open square. Ice core

919 records are marked with a triangle. Marine records are identified with a diamond.

920 Abbreviations for paleoclimate records are as follows: PC = Paru Co; AC = Ahung Co;

921 LZ = Lake Zigetang; SC = Seling Co; TC = Tianmen Cave; NC = Nam Co; MC =

922 Mawmulh Cave; DC = Dandak Cave; DAS = Dasoupu, BC = Bangong Co, SHC =

923 Sahiya Cave.

924

925 **Figure 2:** (a) Detailed digital elevation map of the Nir'pa Co watershed (outlined with a

926 dashed line and shaded blue) showing the position of moraines (while solid lines) and

927 seasonal (dashed blue line) and permanent streams (solid blue line). (b) Expanded view

928   of Nir'pa Co showing the location of inflow (white dashed line) and outflows (solid white

929   line), the delta/shelf at the lakes north end and the location from which cores A-11, A-15

930   and B-15 were collected (white circles). The location of surface samples from the transect

931   are show with green circles. (c) Monthly average temperature (red) and precipitation

932   (blue) at Nir'pa Co (Bird et al., 2014). (d) Grain size results from surface sample transect

933   sites (green circles in 2b).

934

935   **Figure 3:** (a) Excess (red) and supported (blue) ^{210}Pb activities are shown versus depth

936   with ^{137}Cs activities for the top 10 cm of core A-11. Where error bars are not visible, they

937   are smaller than the symbol size. (b) Sediment depth ages based on the CRS age model

938   are shown with the depth at which maximum ^{137}Cs activity occurred (4.5 cm). (c) The

939   composite age model for Nir'pa Co core A-11 with a second order polynomial fit to the

940   ^{210}Pb (red circles) and AMS ^{14}C (blue squares) ages with the ^{137}Cs peak depth shown

941   with a black diamond.

942

943   **Figure 4:** Sedimentological and geochemical results from Nir'pa Co core A-11: (a) dry

944   bulk density; (b) mass accumulation; (c) percent organic matter; (d) organic matter flux;

945   (e) the ratio of elemental carbon to nitrogen; (f) percent biogenic silica (orange) and flux

946   (pink); (g) δ^{13}C of organic matter; (h) δ^{15}N of sedimentary nitrogen. Vertical lines

947   represent the late Holocene mean of each record.

948

949   **Figure 5:** Physical sedimentology and XRF results from Nir'pa Co core A-11: (a)

950   percent lithics and lithic flux; (b) histogram showing the down core abundance

951   distribution of clastic grain sizes; (c) percent sand; (d) percent silt; (e) percent clay on a

952   reversed axis to highlight similarities with %silt; (f) magnetic susceptibility; (g) XRF

953   derived Ti. Vertical lines as in Figure 4.

954

955   **Figure 6:** Comparison of results from Nir'pa Co (a-c) with regional paleoclimate records

956   (d-j). Nir'pa Co (a) %lithics; (b) %sand on a reversed axis; (c) %silt; Paru Co (d) PC1

957   lake level curve (e) PC2 erosion curve; (f) leaf wax hydrogen isotopes; (g) Seling Co

958   δ^{18}O of calcite; (h) Bangong Co δ^{18}O of calcite; (i) Lake Zigetang pollen biome index of

959   relative surface air temperature; (j) Dandak Cave δ^{18}O of calcite. Blue horizontal bars

960   indicate pluvial phases while the gray bar indicates aridity. Vertical lines as in Figure 4

961   and 5.

962

963   **Figure 7:** Comparison of the Paru Co (a-b) and Nir'pa Co (c-d) results with other more

964   distal ISM records from (e) the Arabian Sea marine sediment cores and (f) Qunf Cave

965   δ^{18}O, Oman. Also shown are the (g) El Junco %sand El Niño record and SST

966   reconstructions from (h) the eastern tropical Pacific and (i) Indo-Pacific. Vertical lines as
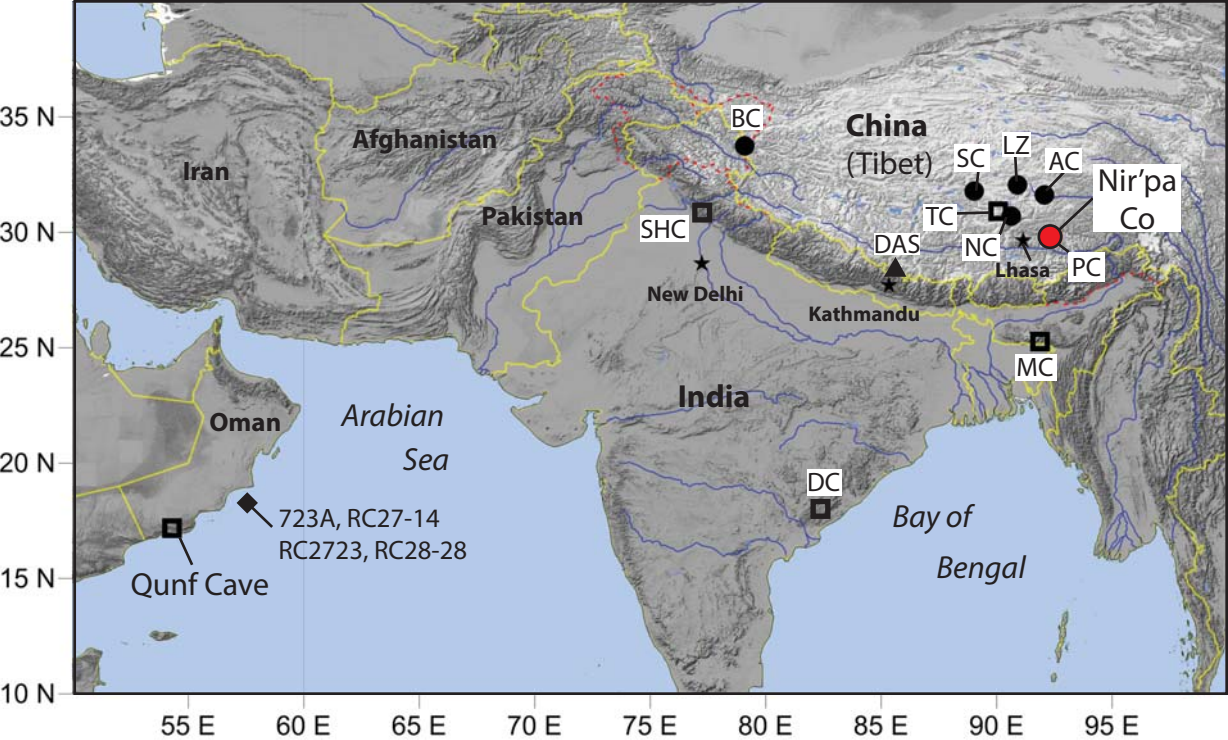
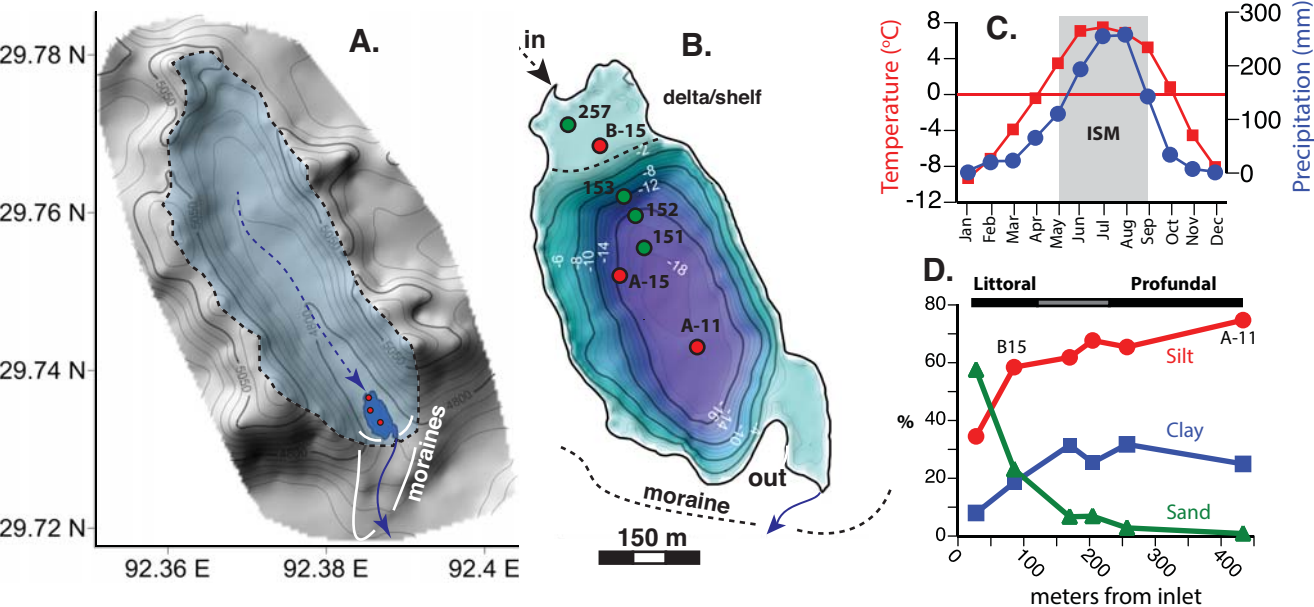967   in Figures 4-6.

Figure 1: Bird et al. (2016)
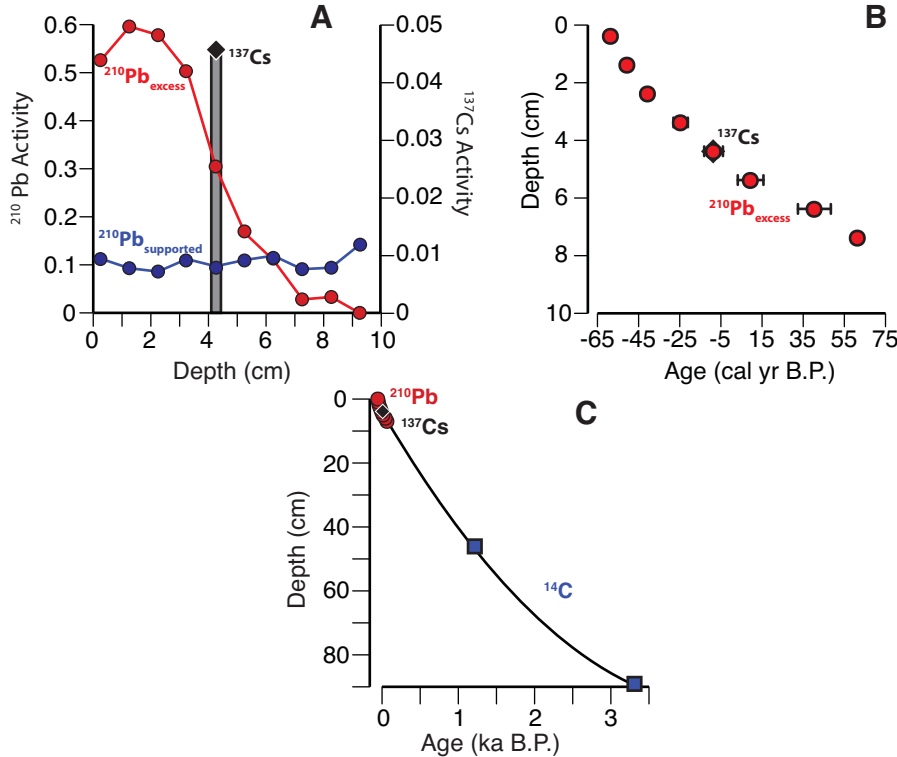
Figure 2 Bird et al. (2016)
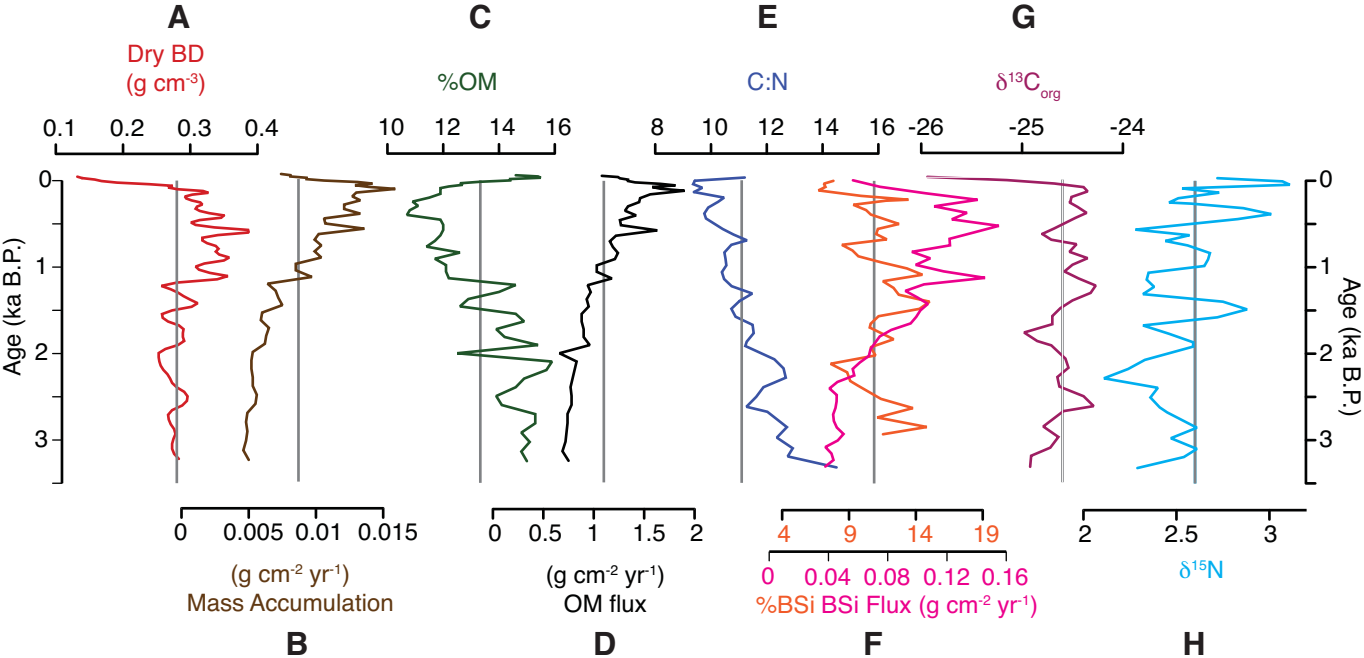
Figure 3: Bird et al. (2016)
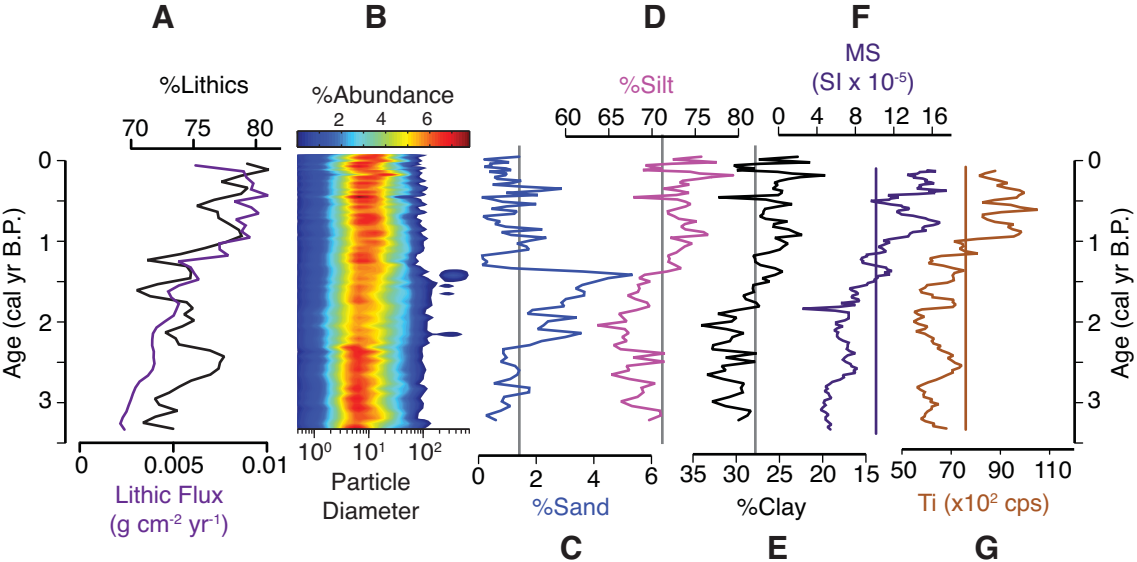
Figure 4: Bird et al. (2016)

Figure 5: Bird et al. (2016)
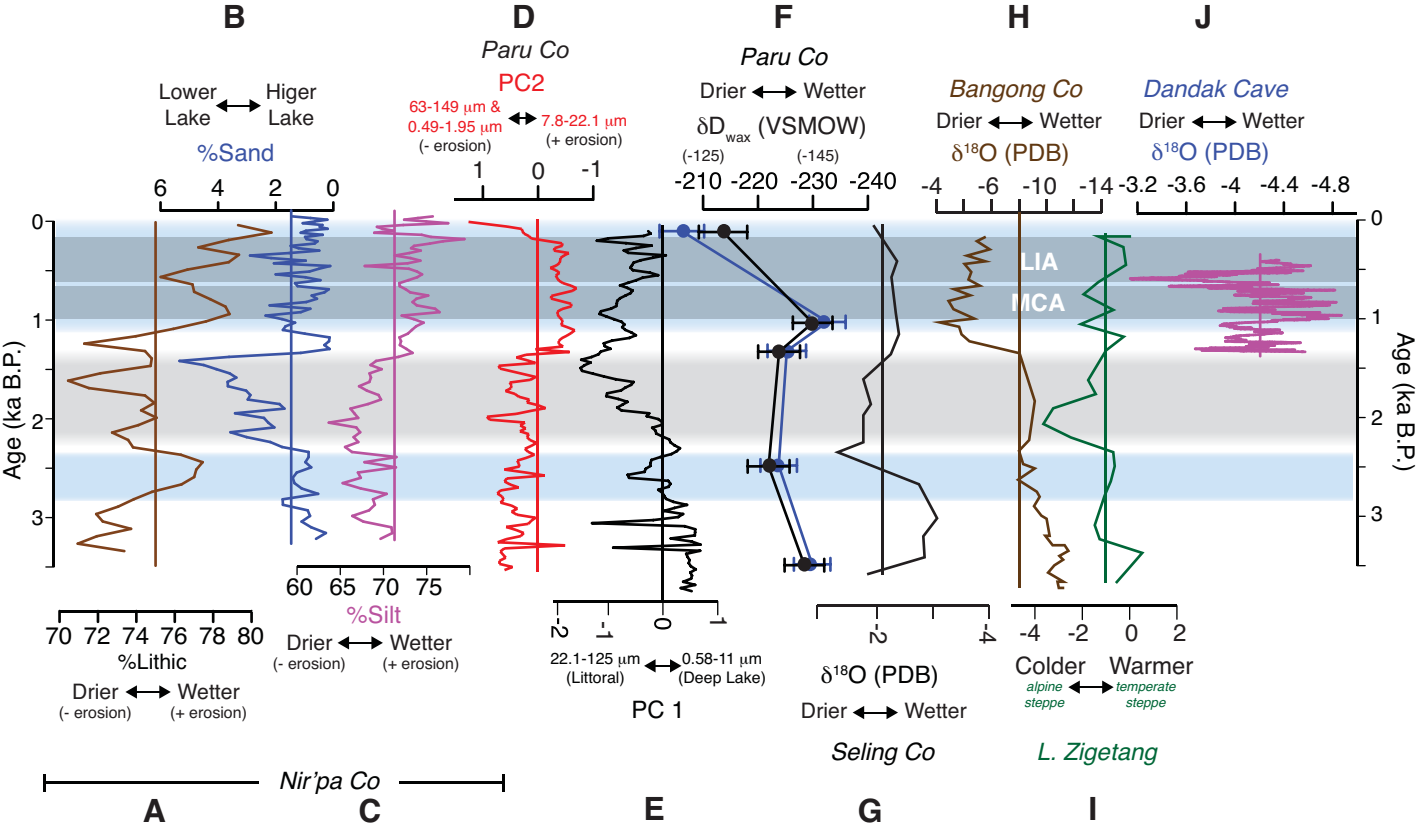
Figure 6: Bird et al. (2016)
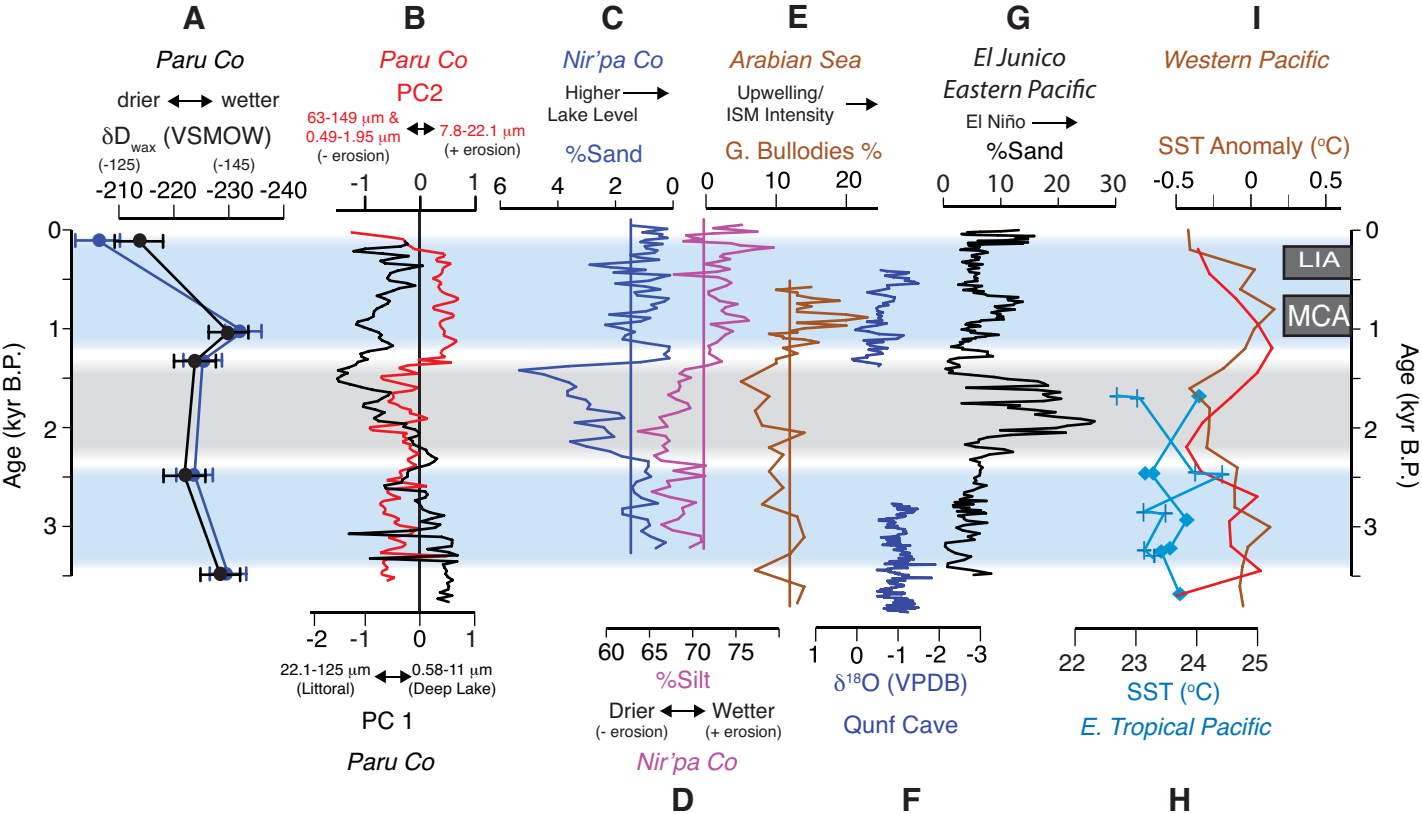
Figure 7: Bird et al. (2016)

Table 1 ^{210}Pb and ^{137}Cs results from Nir'pa Co core A-11.

Mean Depth (cm)	^{210}Pb Activity	±	Supported ^{210}Pb or ^{214}Pb activity (Bq/g)	±	Excess ^{210}Pb (Bq/g)	±	^{137}Cs Activity (Bq/g)	±	cal yr B.P.
0.25	0.64	0.077	0.113	0.014	0.527	0.063	<DET	0	-56
1.25	0.69	0.077	0.093	0.011	0.597	0.066	<DET	0	-48
2.25	0.664	0.0775	0.086	0.012	0.579	0.065	<DET	0	-38
3.25	0.616	0.0735	0.112	0.016	0.504	0.057	<DET	0	-22
4.25	0.4	0.0545	0.097	0.013	0.303	0.042	0.0449	0.0174	-6
5.25	0.277	0.0431	0.110	0.013	0.167	0.030	<DET	0	12
6.25	0.229	0.0417	0.119	0.013	0.110	0.029	<DET	0	43
7.25	0.12	0.02335	0.091	0.009	0.029	0.015	<DET	0	64
8.25	0.128	0.028	0.094	0.010	0.034	0.018	<DET	0	n/a
9.25	0.151	0.03395	0.142	0.014	0.000	0.020	<DET	0	n/a

Table 2 Radiocarbon results from Nir'pa Co cores A-11 & B-15.

UCI AMS #	Core	Depth (cm)	Fraction Modern	±	Δ^{14}C (‰)	±	^{14}C yr B.P.	±	Cal yr B.P.	+/-
104262	A-11	46-47	0.8551	0.0029	-144.9	2.9	1255	30	1210	70/40
104263	A-11	88.5-89.5	0.6812	0.0030	-318.8	3.0	3085	40	3290	92/83
165845	B-15	66-67	0.5809	0.0026	-419.1	2.6	4365	40	4930	60/80
165846	B-15	90-91	0.2931	0.0014	-706.9	1.4	9860	40	11250	90/50